# Interfacial Charge Controlled Lead-Free Perovskite-Polymer Hybrid Structure for Ultra-Sensitive Detection of UV Light

Dali Shao,[*] Weiguang Zhu, Xueqing Liu, Mingxin Li, Guoqing Xin, Jie Lian[*] & Shayla Sawyer[*]

Dr. D. Shao, Dr. X. Liu, Prof. S. Sawyer
Department of Electrical, Computer, and Systems Engineering
Rensselaer Polytechnic Institute
Troy, NY 12180, USA.
E-mail: shaodali828@gmail.com; sawyes@rpi.edu

W. Zhu, Dr. Guoqing Xin, Prof. J. Lian
Department of Mechanical, Aerospace, and Nuclear Engineering
Rensselaer Polytechnic Institute
Troy, NY 12180, USA.
E-mail: lianj@rpi.edu

## Abstract

In this work we demonstrate an ultra-sensitive, visible-blind UV photodetector based on perovskite-polymer hybrid structure. A novel wide-bandgap vacancy-ordered lead-free inorganic perovskite $Cs_2SnCl_6$ with $Nd^{3+}$ doping is employed in the active layer of this hybrid photodetector. Remarkably, with interfacial charge controlled hole-injection operating mechanism, our device achieves a maximum detectivity of $6.3\times10^{15}$ jones at 372 nm, a large linear dynamic range of 118 dB and a fast photoresponse speed (~2.5 µs rise time and ~1.8 µs fall time). The performance is significantly better than most of the existing organic and inorganic semiconductor UV photodetectors reported so far, and its detectivity is closing to one order of magnitude higher than that of the photo-multiplication tube (PMT) in the UV region. In addition, the photodetector demonstrated excellent environmental stability, which is critical for commercial deployment of perovskite based optoelectronic devices. The results

presented in this work open a new route towards development of high-performance optoelectronic devices using perovskite based hybrid nanomaterial systems.

# 1. Introduction

Ultraviolet (UV) photodetector has attracted significant research efforts due to its wide range of applications, such as secure space-to-space communications, pollution monitoring, water sterilization, flame sensing and early missile plume detection.[1-3] Until now most of the commercial UV photodetectors are made from silicon, silicon carbide or gallium nitride p–n junction photodiodes, which are of high cost and their detectivity are usually limited ($<5\times10^{13}$ jones).[4-6] Photo-multiplication tube (PMT) can achieve high detectivity ($\sim3\times10^{14}$ jones) in the UV and visible region, but its applications are limited due to poor UV to visible rejection ratio, high operating voltage (hundreds to thousands of volts), and requirement of large space to install. Therefore, continuous research efforts have been focused in development of novel materials/device architectures that can overcome above issues. Recently, significant progress in organic-inorganic lead halide perovskite materials have enabled various high performance optoelectronic devices including broadband tunable light-emitting diodes (LEDs), highly-sensitive photodetectors, and solar cells that have reached a high power conversion efficiencies above 20%.[7-14] The exciting performance originates from their high carrier mobility, large optical absorption coefficient, as well as long carrier recombination lifetime.[15-17] In particular, hybrid lead halide perovskite based material systems have been demonstrated to be promising for photodetector applications as they offer an inexpensive technology for manufacturing while at the same time be able to achieve excellent detectivities ($10^{13}$-$10^{14}$ jones), large linear dynamic range (over 100 db), and fast response speed (on the order of μs).[10-12]

Despite the stunning progress that has been made on the hybrid lead halide perovskite based photodetectors, their detectivity are still limited as compared to the PMT due to lack of an efficient gain mechanism, and their toxicity together with environmental instability have cast a gloomy shadow over their practical application potency.[18-20] Thus, development of novel device architectures that using environmental stable and Pb-free perovskite materials becomes a pressing need to address the major hurdles for commercial deployment of perovskite-based photodetectors. In this context, Sn, a group-14 element with similar electronic structure to lead, has been firstly considered as the alternative metal for halide perovskite materials. Sn-based perovskites exhibit a narrower bandgap than their Pb analogues with low exciton binding energies, and a longer carrier diffusion length.[21-23] Therefore, Sn-based perovskites are regarded as promising candidate for optoelectronic applications. However, the $Sn^{2+}$ based perovskite is unstable under ambient conditions and easily oxidized from $Sn^{2+}$ to $Sn^{4+}$.[24, 25] In order to further enhance the stability, chemically stable $Sn^{4+}$ based vacancy-ordered double perovskite materials such as $Cs_2SnI_xCl_{6-x}$ and $Cs_2SnCl_{6-x}Br_x$ are recent research focus and have been investigated for energy harvesting, light emitting, and narrow band light detection applications.[26-28] Unfortunately, the detectivity of photodetectors fabricated from $Cs_2SnCl_{6-x}Br_x$ single crystals are limited ($2.71\times10^{10}$ jones) with charge collection narrowing (CCN) mechanism, and the detection range are restricted within the visible region.[27] One possible method to further improve the performance of vacancy-ordered double perovskite based photodetectors is to employ impurity doping, which has been demonstrated to be an effective way to control or improve the material properties, and even to induce new functions for metal halide perovskites.[28] For example, $Zn^{2+}$ doping to $CsPbI_3$ perovskite nanocrystals leads to dramatically improved photoluminescence quantum yield as high as 98.5%.[29] Recently, Zhao and coworkers demonstrated an ultra-stable all-inorganic perovskite solar cell with power conversion efficiency as high as 9.63% using $Sr^{2+}$ doped $CsPbBr_3$ film as the absorber layer.[30]

Herein, we demonstrate a visible-blind perovskite-polymer hybrid photodetector that achieved high detectivity, fast response speed, and large linear dynamic range. The active layer of this photodetector is made by blends of TAPC and novel wide-bandgap, vacancy-ordered, Pb-free inorganic perovskite: $Cs_2SnCl_6$ nanoparticles doped with $Nd^{3+}$ ($Cs_2SnCl_6$:$Nd^{3+}$ NPs). This composite layer acts a photo-sensitive charge-valve that controls the hole injection in the anode. This mechanism is critical for achieving very low noise current and high external quantum efficiency at the same time, leading to an outstanding detectivity in the UV region. It is worth mentioning that the detectivity of this hybrid UV photodetector is significantly better than most of the existing organic and inorganic semiconductor UV photodetectors, and is almost one order of magnitude higher than that of the PMT in the UV region. Moreover, this hybrid UV photodetector is environmental stable, making it promising for high-end photo-detection system applications.

## 2. Results and Discussion

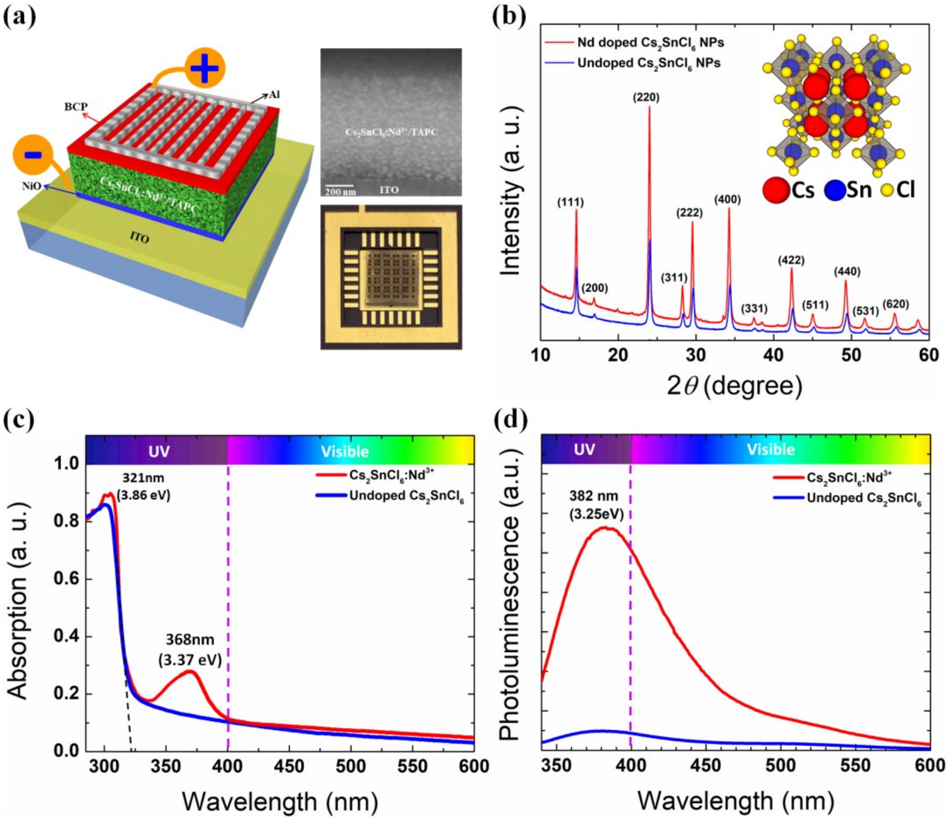

**Figure 1.** Structure of the hybrid UV photodetector and material characterization of $Cs_2SnCl_6$ NPs. a) Three-dimensional schematic illustration of the hybrid UV photodetector. The cross-sectional SEM image on the right side top shows that the $Cs_2SnCl_6:Nd^{3+}$ NPs are uniformly distributed within the TAPC polymer. The right side bottom shows the final device after packaging. b) XRD patterns of the undoped and Nd-doped $Cs_2SnCl_6$ NPs. The major XRD peaks position of $Cs_2SnCl_6:Nd^{3+}$ NPs have been shifted to lower 2θ value as compared to the undoped $Cs_2SnCl_6$ NPs. The inset shows the crystal structure of $Cs_2SnCl_6$, which represent a vacancy-ordered double perovskite structure with isolated [$SnCl_6$] octahedral. c) UV-visible absorption spectra of the $Cs_2SnCl_6$: $Nd^{3+}$ NPs and undoped $Cs_2SnCl_6$ NPs. d) PL spectra of the $Cs_2SnCl_6$: $Nd^{3+}$ NPs and undoped $Cs_2SnCl_6$ NPs.

The three-dimensional schematic illustration of the hybrid UV photodetector is shown in **Figure 1**a. The photoactive layer is made of blends of $Cs_2SnCl_6:Nd^{3+}$ NPs with soluble 1,1-bis[(di-4-tolylamino)phenyl] cyclohexane (TAPC) at the ratio of 3:1 by weight. The TAPC-$Cs_2SnCl_6:Nd^{3+}$ NPs photoactive layer with thickness of ~500nm is sandwiched between a thin layer of NiO with thickness of 10 nm and a thin layer of bathocuproine (BCP) with thickness of 20 nm. The cross-sectional SEM image on the right side top of **Figure 1**a shows that the $Cs_2SnCl_6$:$Nd^{3+}$ NPs are uniformly distributed within the TAPC polymer. The right side bottom of **Figure 1**a shows the final device after packaging. The X-ray diffraction (XRD) patterns of the Nd doped (red line) and undoped (blue line) are shown in Figure 1b. The major XRD peaks position of $Cs_2SnCl_6$:$Nd^{3+}$ NPs have been shifted to lower 2θ values as compared to the undoped $Cs_2SnCl_6$ NPs, indicating the successful incorporation of $Nd^{3+}$ did not change the crystalline form but only expanded the lattice. Because the ionic radius of $Nd^{3+}$ (99 pm) is larger than that of $Sn^{4+}$ (83 pm), the increased lattice constant suggests $Nd^{3+}$ cations replaced $Sn^{4+}$ cations. The inset of **Figure 1**b is the schematic illustration of the crystal structure of $Cs_2SnCl_6$, which represents a vacancy-ordered double perovskite structure with isolated $[SnCl_6]^{2-}$ octahedral bridged by Cs+ cations. To further explore the chemical state of $Nd^{3+}$ in the compound, X-ray photoelectron spectroscopy (XPS) measurement was conducted and the Nd doping concentration is determined to be 1.4%. The typical XPS survey and the high resolution XPS spectra are presented in Figure S1 and S2, respectively. The UV-visible absorption spectra of the undoped and Nd-doped $Cs_2SnCl_6$ NPs thin films were measured under ambient atmosphere and are presented in **Figure 1**c. The $Cs_2SnCl_6$:$Nd^{3+}$ NPs shows a sharp optical absorption edge at 321 nm (3.86 eV), which is due to the intra band transition from the valance band maximum (VBM) to the conduction band minimum (CBM). In addition to the sharp absorption edge at 321 nm, an additional absorption peak at around 368 nm (3.37 eV) is observed. This additional absorption peak would be assigned to transition from the new VBM (VBM′) that introduced by $Nd^{3+}$ doping.[28] Therefore, the “effective optical bandgap” of $Cs_2SnCl_6$:$Nd^{3+}$ is reduced to 3.37eV from 3.86eV of undoped $Cs_2SnCl_6$. The photoluminescence (PL) spectra of the undoped and Nd-doped $Cs_2SnCl_6$ NPs thin films are presented in **Figure 1**d. The $Cs_2SnCl_6$:$Nd^{3+}$ NPs shows a strong and broad PL emission centered at 382 nm (3.25 eV), which agrees with the additional absorption peak observed at 368 nm (3.37 eV). It has been demonstrated in previous studies that doping metal ions into perovskite will normally bring on new, near band edge states, leading to increased density of the lowest excitonic states and dramatically boost the PL intensity.[31,32] Such increase in density of states would also significantly boost the concentration of photo-generated carriers in the device, which is critical for photodetector performance enhancement.

The current density versus voltage (*J*-*V*) characteristics of this photodetector was measured in dark and with 280 nm UV illumination, as shown in **Figure 2**a. The dark current of the photodetector showed a significant rectification characteristic with a rectification ratio of 6362 when biased at ± 5V. Upon UV illumination, the device demonstrates a photocurrent to dark current ratio of ~6 orders of magnitude when biased at -15V, indicating an excellent signal to noise ratio of this photodetector. For comparison, a hybrid photodetector with the same device architecture using undoped $Cs_2SnCl_6$ NPs was fabricated, and the *J*-*V* characteristics are shown in **Figure S3**. Noticed that the photocurrent to dark current ratio of the hybrid photodetector using $Cs_2SnCl_6$:$Nd^{3+}$ NPs is ~4 orders of magnitude higher than that of the reference photodetector fabricated using undoped $Cs_2SnCl_6$ NPs. Such a significant difference in photocurrent to dark current ratio of the two devices originates from their intrinsic different operation mechanisms (interfacial charge controlled hole injection mechanism of $Cs_2SnCl_6$:$Nd^{3+}$ NPs based hybrid photodetector versus typical charge separation and collection of the undoped device), which will be discussed in details later in this article.

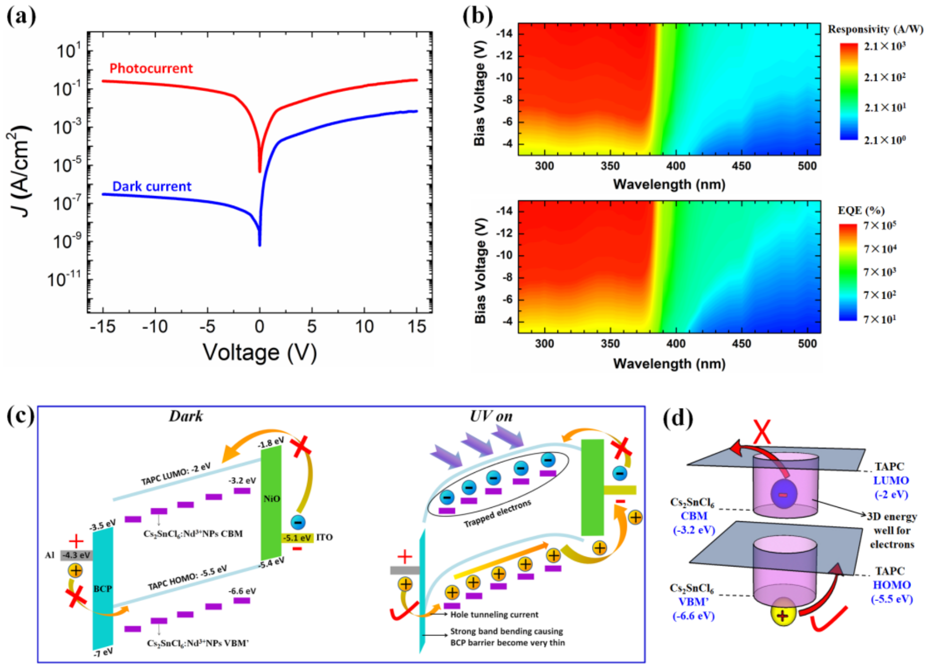

**Figure 2.** Device performance and carrier dynamics of the hybrid UV photodetector. a) Current density versus voltage (*J*-V) characteristics of the hybrid UV photodetector measured in the dark and with 280 nm UV illumination. b) Pseudo-color maps of photoresponsivity spectra (top) and EQE (bottom) of this hybrid UV photodetector measured with varying bias voltages, which show a clear cut-off in both photoresponsivity and EQE at the wavelength of ~380 nm. c) Energy band diagram and carrier dynamics of the hybrid UV photodetector in the dark and under UV illumination. d) Three-dimensional schematic illustration of energy band diagram of the TAPC-$Cs_2SnCl_6:Nd^{3+}$ NPs composite layer under UV excitation. The photogenerated electrons are confined in the energy "well", while the photogenerated holes can freely move in the active layer.

The pseudo-color maps of photoresponsivity spectra (defined as the photo-current per unit incident optical power) and external quantum efficiency (EQE) of this hybrid UV photodetector measured with varying bias voltages are shown in **Figure 2**b top and bottom respectively. A maximum photoresponsivity of 2103.8A/W and EQE of $7.01\times10^5$% are achieved at the wavelength of 372 nm (3.3 eV). To the contrary, the photodetector fabricated with undoped $Cs_2SnCl_6$ NPs shows a much lower photoresponsivity of 0.083A/W and EQE of 32.6% at 316 nm, as shown in **Figure S4**. From the pseudo-color maps in Figure 2b, there is a clear cut-off in both photoresponsivity and EQE at the wavelength of ~380 nm. This cut-off wavelength agrees with the additional 368 nm absorption peak observed in the optical absorption spectrum that shown in Figure 1e.

To understand the high photoresponsivity/EQE of this photodetector, we can refer to the schematic energy band diagram in **Figure 2**c. When in dark and under reverse bias condition, the BCP's hole blocking ability, together with the large band offset between the HOMO of BCP (-7 eV) and work function of Al (-4.3 eV), can effectively impede hole injection from the Al electrode.[33,34] Similarly, electron injection from the ITO can be greatly suppressed due to NiO's electron blocking ability together with the large band offset between the work function of ITO (-5.1 eV) and the conduction band minimum of NiO (-1.8eV).[35-37] Such excellent carrier injection blocking capability from both top and bottom electrodes under reverse biased condition can effectively suppress the dark current, which is critical to achieve low noise and high detectivity. Upon UV illumination, the $Cs_2SnCl_6$:$Nd^{3+}$ NPs in the active layer absorb incident photons and generate electron-hole pairs. The photogenerated holes from $Cs_2SnCl_6$: $Nd^{3+}$ NPs can be transported through TAPC/NiO and finally be collected from the ITO under external bias voltage. To the contrary, the photogenerated electrons remain confined in the $Cs_2SnCl_6$: $Nd^{3+}$ NPs due to lack of a percolation network for electrons as well as the strong electron confinement effect of the "energy well" formed in the TAPC-$Cs_2SnCl_6$: $Nd^{3+}$ NPs composite layer (large band offset between the LUMO of TAPC and CBM of $Cs_2SnCl_6$, together with TAPC's electron blocking capability can effectively confine the photogenerated electrons in the composite layer), as illustrated in **Figure 2**d.[38-40] The confined electrons accumulate and quickly shift the LUMO of the TAPC downwards and align the Fermi level of the composite layer with that of the Al. Therefore, the BCP as hole-injection barrier becomes very thin due to the band bending and the holes can easily tunnel through it with assistance of a small reverse bias, resulting a dramatic increase of photo-induced injection of hole-tunneling current (which is the main contributor for the high photoresponsivity and EQE). Accordingly, the Al-BCP interface acts as a 'switch' for hole-tunneling current injection that is controlled by the TAPC-$Cs_2SnCl_6$:$Nd^{3+}$ NPs composite layer, and the incident photon can turn on this switch. The energy band bending at the BCP layer is determined by the energy barrier change $\Delta\Phi$ at the Al-BCP interface, which is a linear function of trapped electron density $n_{trap}$ in the TAPC-$Cs_2SnCl_6$:$Nd^{3+}$ NPs composite layer. The injection current follows an exponential relationship with the energy barrier change according to the Richardson-Dushman equation:

$$J \propto \exp\,(-\frac{\Delta\Phi}{kT}) \propto \exp\,(-\frac{n_{trap}}{kT})$$

where $k$ is the Boltzmann constant and $T$ is the temperature. For the reference photodetector, however, the high intrinsic band gap (3.86 eV) and lower density of the lowest excitonic states of the undoped $Cs_2SnCl_6$ NPs making its photo-generation rate much lower as compared to the $Cs_2SnCl_6$:$Nd^{3+}$ NPs based device, resulting in much less trapped electrons in the active layer and hence not be able to generate strong enough band bending at the Al-BCP interfaces to trigger the injection of hole tunneling current.

As the operation of this hybrid UV photodetector depends on the electron confinement and hole injection/transport in the TAPC-$Cs_2SnCl_6$: $Nd^{3+}$ NPs composite layer, hole-only and electron-only devices that employ TAPC-$Cs_2SnCl_6$: $Nd^{3+}$ NPs as active layer were fabricated for verification of the electron confinement capability and hole transport properties of the TAPC-$Cs_2SnCl_6$:$Nd^{3+}$ NPs composite layer. The electron-only device has a structure of $Cs_2CO_3$/TAPC-$Cs_2SnCl_6$:$Nd^{3+}$ NPs/BCP and the hole-only device has a structure of NiO/TAPC-$Cs_2SnCl_6$: $Nd^{3+}$ NPs/NiO. For the electron-only device, both the $Cs_2CO_3$ layer and BCP layer are electron transport layers with the capability of blocking holes, therefore only electrons can be injected.[34] Similarly, NiO has been demonstrated as an effective hole injection layer with good capability of blocking electrons, therefore only holes can be injected into the hole-only device. The measured dark current of the two device structures are shown in **Figure S5**, from which we can see that the current density in hole-only device is more than 4 orders of magnitude higher than that of the electron-only device. This verifies that electrons can hardly move in the active layer while the holes can freely transport in the device structure.

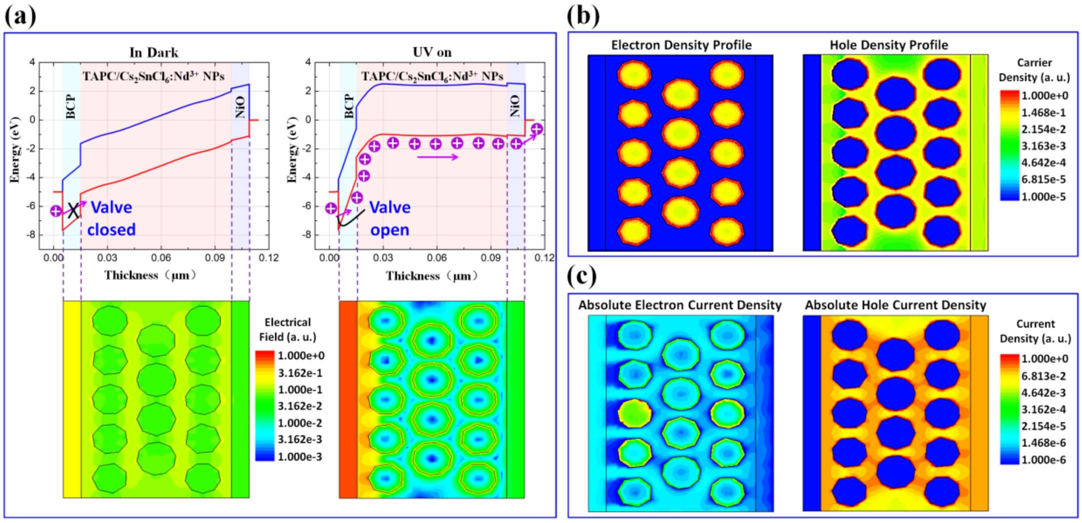

**Figure 3.** Device modeling of the hybrid UV photodetector. a) Simulated energy band diagram and local electrical field intensity of the device modeled in both dark and light condition. Under UV illumination, the energy barrier for holes at anode become very thin due to the strong band bending in the BCP layer, causing significantly increase of the hole tunneling current. b) Electron and hole density profiles of the device under UV illumination. The photo-generated electrons are very well confined in the $Cs_2SnCl_6:Nd^{3+}$ NPs while the photo-generated holes can drift and be collected at cathode under external bias. c) Absolute electron and hole current density of the device under UV illumination. The hole current density is almost 6 orders of magnitude higher than that of the electron current.

For a better understanding and visualization of the above discussed interfacial charge controlled hole injection mechanism, device simulation was carried out using Synopsys Sentaurus TCAD. The details of the simulation setup can be found in the Experimental Section and the structure of the simulated device is presented in **Figure S6**. In this case, a simplified model of this hybrid UV photodetector is employed for a better visualization of the device operating mechanism, including: energy band bending, local electric field and carriers distribution, as well as absolute electron/hole current density profile. **Figure 3**a shows the simulated energy band diagram and local electrical field intensity of the device modeled in both dark and light condition. UV light at 280 nm wavelength with light intensity of 100 mW/cm$^2$ is used in the simulation. It can be seen that the energy band bending at BCP layer become very sharp under UV illumination, resulting significantly increase of electric field across the BCP layer. Such a strong band bending and enhancement of the electric field in the BCP layer is due to a quick accumulation of photo-generated electrons that confined in the

$Cs_2SnCl_6$ NPs, as demonstrated in **Figure 3**b. Noted that the photo-generated holes are not confined in the active layer and can drift toward the cathode under external bias. The band bending in the BCP layer is strong enough to introduce significant increase of hole-tunneling current, as shown in the simulated absolute electron/hole current density profiles in **Figure 3**c. From the normalized current density scale bar, it clearly show that under UV illumination the absolute hole current density in the device is almost 6 orders of magnitude higher than that of the electron current, demonstrating that the high gain of this hybrid UV photodetector is originated from the injected hole-tunneling current. The normalized absolute total current (absolute electron current + absolute hole current) of the device without and with UV illumination are shown in **Figure S7**. The above simulated results logically explained the extremely high external quantum efficiency of this device.

For practical applications, such as image sensors and illumination meters, having a constant responsivity over a wide range of light intensity is an important figure of merit for a photodetector. The linear dynamic range (LDR) of a photodetector indicates that within a certain range, the photodetector has a linear response to varying incident light intensity and can keep a constant responsivity. LDR is expressed as:[10,41]

$$\mathrm{LDR} = 20\log\left(P_{sat}/P_{low}\right)$$

where $P_{sat}$ and $P_{low}$ are the upper and lower limit of the incident light intensities that beyond this range the photocurrent begins to deviate from linearity. The LDR of the hybrid UV photodetector was characterized by measuring the photocurrent at a fixed frequency of 100 Hz under 280 nm UV illumination with varying light intensity from $4.5\times10^{-2}$ W/cm$^2$ to $1.0\times10^{-9}$ W/cm$^2$, as shown in **Figure 4**a. Our device shows a linear photoresponse within the incident light intensity range from $4.5\times10^{-2}$ W/cm$^2$ to $5.6\times10^{-8}$ W/cm$^2$, corresponding to a LDR of ~118 dB. This is comparable with Si photodetectors and are much better than other types of photodetectors such as GaN (50 dB) and InGaAs (66 dB).[10] The inset of **Figure 4**a is the corresponding responsivity measured within above light intensity range, which shows a good consistency of the responsivity for light intensity range from $4.5\times10^{-2}$ W/cm$^2$ to $5.6\times10^{-8}$ W/cm$^2$.

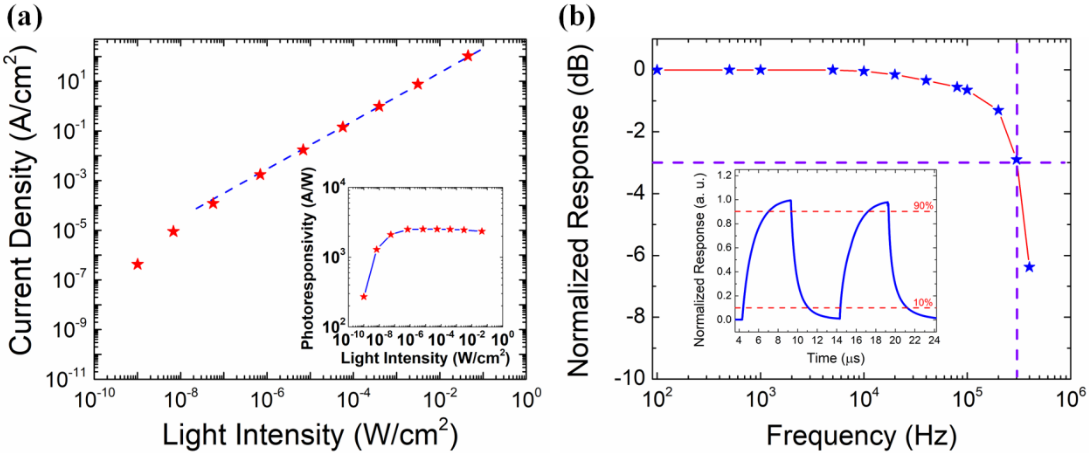

**Figure 4.** Linear dynamic range and transient response of the hybrid UV photodetector. a) Photocurrent density measured at varying light intensity from $4.5\times10^{-2}$ W/cm$^2$ to $1.0\times10^{-9}$ W/cm$^2$. The inset shows a good consistency of the responsivity at varying light intensity. b) Normalized photoresponse vs light pulse frequency for the device. Inset: transient photoresponse of the device.

The response speed is another important parameter for photodetectors. **Figure 4**b shows the normalized response vs light pulse frequency for the device. The 3-dB bandwidth is measured to be ~300 kHz. The inset of **Figure 4**b shows the transient response of the device, which was measured under a 280 nm short pulse (100 kHz) light from a LED. The rise time (output signal changing from 10% to 90% of the peak output value) and the decay time (output signal changing from 90% to 10% of the peak output value) of the photocurrent are 2.5 μs and 1.8 μs, respectively. Noted that this response speed is faster than most of the organic, quantum dot and hybrid photodetectors (typically on the order of millisecond).[42-48]

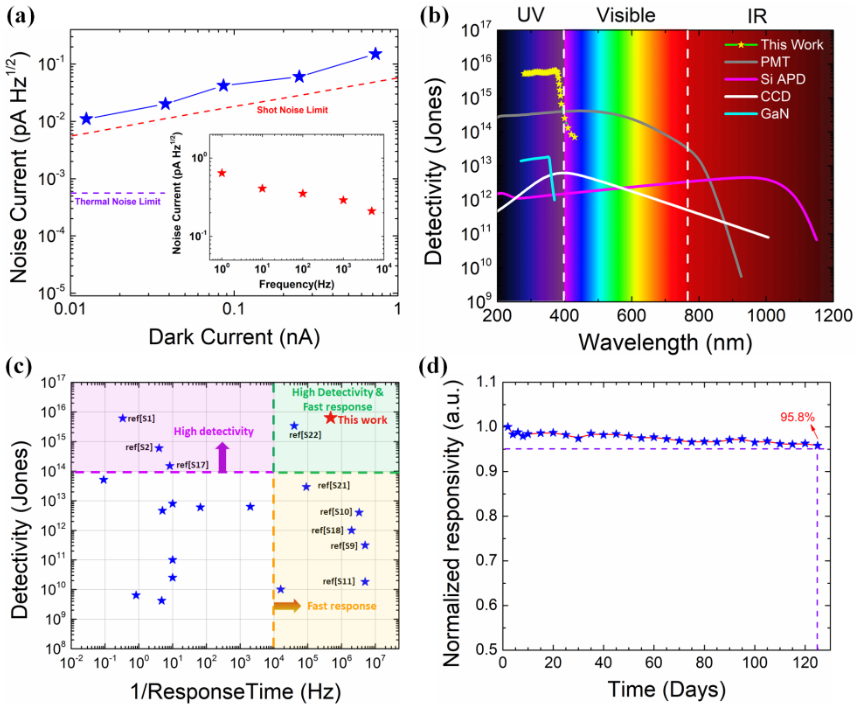

**Figure 5.** Noise current, detectivity, overall performance, and environmental stability of the hybrid UV photodetector. a) Noise current measured at different dark current levels. Inset: Noise current measured at various frequencies in the range from 1 Hz to 5K Hz. b) Specific detectivity spectrum of the hybrid UV photodetector and its comparison to different types of commercial photodetectors. c) Overall performance of the hybrid UV photodetector in this work in comparison with various state-of-the-art UV photodetectors in terms of maximum detectivity and the response speed. The detectivity and response time data in the plot are presented in **Table S1**. d) Time-dependent responsivity stability test.

The specific detectivity is one of the most important figure-of-merits for photodetectors. It characterizes the capability of a photodetector to detect the weakest light signal. The specific detectivity ($D^*$) can be expressed as:[4,41]

$$D^* = \frac{(AB)^{1/2}}{\mathrm{NEP}}$$

where the NEP = $i_n/R$ is the noise equivalent power, $B$ is the bandwidth, $A$ is the area of the device, $i_\mathrm{n}$ is the measured noise current, and $R$ is the photoresponsivity of the photodetector. The dark current of our device is less than 100 pA at -15 V because of the outstanding carrier injection blocking capability at both cathode and anode, which ensures a very low shot noise. To include other possible noise, such as flicker noise and thermal noise, the total noise current of the photodetector was directly measured with an SR830 lock-in amplifier at different dark current levels and at various frequencies (range from 1 Hz to 5 kHz), as presented in **Figure 5**a. The measured noise current of this hybrid photodetector is mainly dominated by shot noise and is barely sensitive to frequency modulation, indicating a negligible 1/f noise of our device. The detectivity of this hybrid UV photodetector is calculated at different wavelengths with the measured noise current and responsivity at -15 V bias, and the results are plotted in **Figure 5**b. For comparison, we also include the detectivity spectra of a Si-avalanche photodiode (APD), a GaN UV photodetector, a photomultiplier tube (PMT). Remarkably, the maximum specific detectivity of our device reaches to ~$6.3\times10^{15}$ jones at 372 nm, and is consistently above $5\times10^{15}$ jones in the UV region for wavelength from 380 nm to 280 nm. This is at least 2-3 orders of magnitude higher than those of Si-APD and GaN photodetectors, and is more than one order of magnitude higher than that of the PMT in the UV region. The overall performance of our hybrid UV photodetector in terms of detectivity versus response speed is compared with various other types of UV photodetectors in **Table S1**, and the data are plotted in **Figure 5**c. Obviously, our photodetector demonstrated high detectivity and fast response speed at the same time. The responsivity of the hybrid photodetector over time is shown in **Figure 5**d, which shows that the device performance can be maintained above 95% of its initial value for more than four month after storage in 30% relative humidity conditions.

In summary, we have demonstrated a perovskite-polymer hybrid UV photodetector that showing excellent photodetection properties including high external quantum efficiency and detectivity, fast response speed, and large linear dynamic range. In particular, the detectivity of this device surpass the commercial PMT by almost one order of magnitude, and is significantly better than most of the organic, inorganic or hybrid UV photodetectors. The high performance originates from the interfacial charge controlled carrier injection mechanism, which is the key to achieve high external quantum efficiency and significantly suppressed dark current at the same time. In addition, this hybrid UV photodetector demonstrated excellent environmental stability, which is of great importance for practical applications. The rationale presented in this work can be utilized as a future guideline to design high-performance optoelectronics with perovskite-polymer hybrid nanomaterial systems.

# 4. Experimental Section

The synthesis of the $Cs_2SnCl_6$:$Nd^{3+}$ NPs were using a typical hydrothermal method. CsCl (337 mg, 2 mmol) was dissolved in 5 mL methanol. In a separate 25 mL beaker, $SnCl_4 \cdot 5H_2O$ (351 mg, 1 mmol) with $NdCl_3$ (31.5 mg, 0.1 mmol) was mixed and dissolved in 5 mL methanol to afford a clear transparent solution. Addition of the alcoholic mixture solution to the CsCl solution under vigorous stirring at room temperature led to spontaneous precipitation of white powder. The mixture was stirred for a further 30 min to ensure completion of the reaction, after which the solid was washed by methanol in a centrifuge at 3000 RPM for 5 min twice. Then the obtained powder was dried in an oven at 80 °C overnight. The XRD spectrum of the Bi doped $Cs_2SnCl_6$ NPs was measured using a Panalytical X'Pert Pro system (Westborough, MA, USA) with a copper target ($K_\alpha$= 0.15406 nm) and a step size of 0.0131°. The UV-visible absorption spectrum was measured using Shimadzu UV-Vis 2550 spectrophotometer and the X- XPS measurement was carried out using a PHI 5000 Versa Probe system.

For the device fabrication, the ITO substrates were first cleaned with acetone and isopropanol in an ultrasonic cleaner and subsequently rinsed with deionized water, and blown dry with $N_2$ gas. Then, a thin layer of NiO with thickness of approximate 10 nm is deposited onto the ITO substrate using thermal evaporation with a deposition rate at ~0.5 Å/s. The NiO acts as a hole transport/electron blocking layer. The TAPC-$Cs_2SnCl_6$:$Nd^{3+}$ NPs blends were dispersed in dichlorobenzene solvent (51 mg/mL) and spin-coated to the substrate at 3000 rpm. Then, a 20 nm thick bathocuproine (BCP) layer was deposited to cover the TAPC-

$Cs_2SnCl_6$:Bi NPs composite layer through thermal evaporation, which acts as an electron transport/hole blocking layer. 100 nm Al was then deposited as top electrode of the device using e-Beam evaporator. Finally, the hybrid photodetector was wire bonded using Epo-Tek H20E conductive epoxy. The active device area is 150 µm ×150 µm.

For the device characterization, the I-V characteristics of the photodetector were measured using a HP4155B semiconductor parameter analyser and a UV LED with centre peak wavelength at 280 nm. The output optical power density of the 280 nm UV LED was adjusted by a current injection controller and verified using a commercial Si photodetector. The photoresponsivity spectra of the devices were measured using a Shimadzu UV-Vis 2550 spectrophotometer in connection with optical power meter. To determine the noise current of this hybrid UV photodetector, SR830 DSP dual phase lock-in amplifier lock-in amplifier was used to measure the background noise level of the device. The testing was carried out in an electrically shielded and optically sealed probe station, and on a floating table to minimize the vibrational noise.

Synopsys Sentaurus TCAD package was used to study the electric field distribution and carrier dynamics of the device. The detailed dimensions of the simulated device can be referred to supplementary Figure 1. Polygons with varying angles and side numbers were used to model the $Cs_2SnCl_6$:$Nd^{3+}$ NPs. The simulated device was illuminated by an unpolarized normally incident light located 100 nm away to the device. The incident light has a wavelength of 280 nm with light intensity of $100mW/cm^2$. The ray tracing optical solver was used to calculate the optical generation rate in the device, which was coupled with the electrical simulation using the drift-diffusion transport model. Physical models including thermionic, high-field saturation, Shockley-Read-Hall (SRH) recombination, and barrier tunneling were activated in the simulation. The energy band diagram and the profiles of electric field, carrier density, and current density were visualized at the condition when the voltage applied on the simulated device was ramped to 5V. The energy band diagram was plotted at a cross section perpendicular to each layer of the simulated device without cutting through $Cs_2SnCl_6$ NPs. Symmetric boundary conditions were used in the direction perpendicular to the light incidence, while along the light incidence constant reflectivity boundary conditions were specified, with the rays incident on the contact with positive bias having no reflection and the rays incident on the contact grounded totally reflected back into the device structure.

## Supporting Information

Supporting Information is available from the Wiley Online Library or from the author.

## Acknowledgments

Dr. Sawyer and Dr. Shao acknowledges funding support from New Knowledge and Innovation Program (KIP) Seed Grant program at Rensselaer Polytechnic Institute. Dr. Lian acknowledges the support from the Center for Performance and Design of Nuclear Waste Forms and Containers, an Energy Frontier Research Center funded by the U.S. Department of Energy, Office of Science, Basic Energy Sciences under Award # DE-SC0016584. D.S. and W.Z. performed the material synthesis, device fabrication, data collection and analysis. All authors discussed the results, prepared and commented on the manuscript. J.L. and S.S. planned and supervised the project.

## Conflict of Interest

All the authors declare that they have no competing interests.

## Keywords

Inorganic perovskite, $Cs_2SnCl_6$, Neodymium, UV photodetector, hole injection

# References

[1] X. Liu, L. Gu, Q. Zhang, J. Wu, Y. Long, Z. Fan, *Nat. Commun.* **2014**, 5, 4007.

[2] T. Mueller, F. Xia, P. Avouris, *Nat. Photon.* **2010**, 4, 297.

[3] C.-H. Liu, Y.-C. Chang, T. B. Norris, Z. Zhong, *Nat. Nanotechnol.* **2014**, 9, 273.

[4] F. Guo, B. Yang, Y. Yuan, Z. Xiao, Q. Dong, Y. Bi, J. Huang, *Nat. Nanotechnol.* **2012**, 7, 798.

[5] D. Shao, J. Gao, P. Chow, H. Sun, G. Xin, P. Sharma, J. Lian, N. A. Koratkar, S. Sawyer, *Nano Lett.* **2015**, 15, 3787.

[6] M. C. Chen, J. K. Sheu, M. L. Lee, C. J. Tun, G. C. Chi, *Appl. Phys. Lett.* **2006**, 89, 183509.

[7] X. Hu, X. Zhang, L. Liang, J. Bao, S. Li, W. Yang, Y. Xie, *Adv. Funct. Mater.* **2014**, 24, 7373.

[8] Z.-K. Tan, R. S. Moghaddam, M. L. Lai, P. Docampo, R. Higler, F. Deschler, M. Price, A. Sadhanala, L. M. Pazos, D. Credgington, F. Hanusch, T. Bein, H. J. Snaith, R. H. Friend, *Nat. Nanotechnol.* **2014**, 9, 687.

[9] G. Li, Z.-K. Tan, D. Di, M. L. Lai, L. Jiang, J. H.-W. Lim, R. H. Friend, N. C. Greenham, *Nano Lett.* **2015**, 15, 2640.

[10] L. Dou, Y. Yang, J. You, Z. Hong, W.-H. Chang, G. Li, Y. Yang, *Nat. Commun.* **2014**, 5, 5404.

[11] M. I. Saidaminov, V. Adinolfi, R. Comin, A. L. Abdelhady, W. Peng, I. Dursun, M. Yuan, S. Hoogland, E. H. Sargent, O. M. Bakr, *Nat. Commun.* **2015**, 6, 8724.

[12] Y. Fang, Q. Dong, Y. Shao, Y. Yuan, J. Huang, *Nat. Photonics* **2015**, 9, 679.

[13] W. S. Yang, J. H. Noh, N. J. Jeon, Y. C. Kim, S. Ryu, J. Seo, S. I. Seok, *Science* **2015**,

348, 1234.

[14] N. Arora, M. I. Dar, A. Hinderhofer, N. Pellet, F. Schreiber, S. M. Zakeeruddin, M. Grätzel, *Science* **2017**, 358, 768.

[15] S. D. Stranks, G. E. Eperon, G. Grancini, C. Menelaou, M. J. P. Alcocer, T. Leijtens, L. M. Herz, A. Petrozza, H. J. Snaith, *Science* **2013**, 342, 341.

[16] D. Shi, V. Adinolfi, R. Comin, M. Yuan, E. Alarousu, A. Buin, Y. Chen, S. Hoogland, A. Rothenberger, K. Katsiev, Y. Losovyj, X. Zhang, P. A. Dowben, O. F. Mohammed, E. H. Sargent, O. M. Bakr, *Science* **2015**, 347, 519.

[17] J. H. Heo, S. H. Im, J. H. Noh, T. N. Mandal, C.-S. Lim, J. A. Chang, Y. H. Lee, H.-J. Kim, A. Sarkar, M. K. Nazeeruddin, M. Grätzel, S. I. Seok, *Nat. Photon.* **2013**, 7, 487.

[18] X. M. Li, F. Cao, D. J. Yu, J. Chen, Z. G. Sun, Y. L. Shen, Y. Zhu, L. Wang, Y. Wei, Y. Wu, H. B. Zeng, *Small*, **2017**, 13, 1603996.

[19] M. Y. Leng, Z. W. Chen, Y. Yang, Z. Li, K. Zeng, K. H. Li, G. D. Niu, Y. S. He, Q. C. Zhou, J. Tang, Lead-Free, *Angew. Chem. Int. Ed.* **2016**, 55, 15012.

[20] A. Babayigit, A. Ethirajan, M. Muller, B. Conings, *Nat. Mater.* **2016**, 15, 247.

[21] I. Chung, J.-H. Song, J. Im, J. Androulakis, C. D. Malliakas, H. Li, A. J. Freeman, J. T. Kenney, M. G. Kanatzidis, *J. Am. Chem. Soc.* **2012**, 134, 8579.

[22] L.-Y. Huang, W. R. L. Lambrecht, *Phys. Rev. B* **2013**, 88, 165203.

[23] X. Wang, T. Zhang, Y. Lou, Y. Zhao, *Mater. Chem. Front.* **2019**, 3, 365.

[24] N. K. Noel, S. D. Stranks, A. Abate, C. Wehrenfennig, S. Guarnera, A. Haghighirad, A. Sadhanala, G. E. Eperon, S. K. Pathak, M. B. Johnston, A. Petrozza, L. M. Herz, H. J. Snaith, *Energy Environ. Sci.* **2014**, **7**, 3061.

[25] F. Hao, C. C. Stoumpos, D. H. Cao, R. P. H. Chang, M. G. Kanatzidis, *Nature Photon.* **2014**, 8, 489.

[26] B. Lee, C. C. Stoumpos, N. Zhou, F. Hao, C. Malliakas, C.-Y. Yeh, T. J. Marks, M. G. Kanatzidis, R. P. H. Chang, *J. Am. Chem. Soc.* **2014**, 136, 15379.

[27] J. Zhou, J. Luo, X. Rong, P. Wei, M. S. Molokeev, Y. Huang, J. Zhao, Q. Liu, X. Zhang J. Tang, Z. Xia, *Adv. Optical Mater.* **2019**, 1900139.

[28] Z. Tan, J. Li, C. Zhang, Z. Li, Q. Hu, Z. Xiao, T. Kamiya, H. Hosono, G. Niu, E. Lifshitz, Y. Cheng, J. Tang, *Adv. Funct. Mater.* **2018**, 28, 1801131.

[29] X. Shen, Y. Zhang, S. V. Kershaw, T. Li, C. Wang, X. Zhang, W. Wang, D. Li, Y. Wang, M. Lu, L. Zhang, C. Sun, D. Zhao, G. Qin, X. Bai, W. W. Yu, A. L. Rogach, *Nano Lett.* **2019**, 19, 1552.

[30] Y. Zhao, Y. Wang, J. Duan, X. Yang, Q. Tang, *J. Mater. Chem. A* **2019**, 7, 6877.

[31] J. Yao, J. Ge, B.-N. Han, K.-H. Wang, H.-B. Yao, H.-L. Yu, J.-H. Li, B.-S. Zhu, J. Song, C. Chen, Q. Zhang, H. Zeng, Y. Luo, S.-H. Y, J. Am. Chem. Soc., **2018**, 140, 3626.

[32] J.-P. Ma, Y.-M. Chen, L.-M. Zhang, S. Guo, J.-D. Liu, H. Li, B. Ye, Z. Li, Y. Zhou, B.-B. Zhang, O. M. Bakr, J. Zhang, H.-T. Sun, *J. Mater. Chem. C* 2019, 7, 3037.

[33] Y. Divayana, B. J. Chen, X. W. Sun, K. S. Sarma, *App. Phys. Lett.* **2006**, 88, 083508.

[34] Q. Wang, Y. Shao, Q. Dong, Z. Xiao, Y. Yuan, J. Huang, *Energy Environ. Sci.* **2014**, 7, 2359.

[35] K.-Ch. Wang, P.-S. Shen, M.-H. Li, S. Chen, M.-W. Lin, P. Chen, T.-F. Guo, ACS *Appl. Mater. Interfaces* **2014**, 6, 11851.

[36] M. D. Irwin, D. B. Buchholz, A. W. Hains, R. P. H. Chang, T. J. Marks, *PNAS* **2008**, 105, 2783.

[37] X. Yin, Z. Yao, Q. Luo, X. Dai, Y. Zhou, Y. Zhang, S. Luo, J. Li, N. Wang, H. Lin, *ACS Appl. Mater. Interfaces* **2017**, 9, 2439.

[38] G. Liaptsis K. Meerholz, *Adv. Func. Mater.* **2013**, 23, 359.

[39] A. Kaltzoglou, M. Antoniadou, A. G. Kontos, C. C. Stoumpos, D. Pergant, E. Siranidi, V. Raptis, K. Trohidou, V. Psycharis, M. G. Kanatzidis, P. Falaras, *J. Phys. Chem. C* **2016**, 120, 11777.

[40] A. E Maughan, A. M. Ganose, D. O. Scanlon, J. R. Neilson, *Chem. Mater.* **2019**, 31, 1184.

[41] C. Bao, Z. Chen, Y. Fang, H. Wei, Y. Deng, X. Xiao, L. Li, J. Huang, *Adv. Mater.* **2017**, 29, 1703209.

[42] H. Zhang, X. Dai, N. Guan, A. Messanvi, V. Neplokh, V. Piazza, M. Vallo, C. Bougerol, F. H. Julien, A. Babichev, N. Cavassilas, M. Bescond, F. Michelini, M. Foldyna, E. Gautier, C. Durand, J. Eymery, M. Tchernycheva. *ACS Appl. Mater. Interfaces* **2016**, 8, 26198.

[43] J. Wu, L. Y. Lin, *Adv. Opt. Mater.* **2015**, 3, 1530.

[44] X.-X. Yu, H. Yin, H.-X. Li, W. Zhang, H. Zhao, C. Li, M.-Q. Zhu, *Nano Energy* **2017**, 34, 155.

[45] P. Yu, K. Hu, H. Chen, L Zheng, X. Fang, *Adv. Funct. Mater.* **2017**, 27, 1703166.

[46] X. Wang, Y. Dai, R. Liu, X. He, S. Li, Z. L. Wang, *ACS Nano* **2017**, 11, 8339.

[47] M. I. Saidaminov, M. A. Haque, J. Almutlaq, S. Sarmah, X.-H. Miao, R. Begum, A. A. Zhumekenov, I. Dursun, N. Cho, B. Murali, O. F. Mohammed, T. Wu, O. M. Bakr, *Adv. Opt. Mater.* **2017**, 5, 1600704.

[48] W. Peng, X. Wang, R. Yu, Y. Dai, H. Zou, A. C. Wang, Y. He, Z. L. Wang, *Adv. Mater.* **2017**, 29, 1606698.